SUPPORTING INFORMATION

Modeling the global fate and transport of perfluorooctanoic acid (PFOA) and perfluorooctanoate (PFO) emitted from direct sources using a multi-species mass balance model

James M. Armitage,[†] Matthew MacLeod,[§] Ian T. Cousins,[†]*

[†] Department of Applied Environmental Science (ITM), Stockholm University, SE-10691 Stockholm, Sweden

[§] Institute for Chemical and Bioengineering, Swiss Federal Institute of Technology, ETH Zurich, HCI G129, CH-8093 Zürich, Switzerland.

* corresponding author: ian.cousins@itm.su.se; +46 (0)8 16 4012

Contents: 34 pages, 8 figures, 6 tables

S1. Distribution ratio approach

The distribution ratio approach calculates a weighted-average of the partition coefficients of each species of the molecule for a given physical-chemical property. The weighted-average is based on the ratio of ionic to nonionic forms of the substance, estimated using the Henderson-Hasselbalch relationship so that,

$$Ratio = 10^{[pH(i)-pKa]} \quad \text{(S1)}$$

where pH(i) is the pH of the environmental media. The distribution of PFO(A) in aqueous media (e.g. organic carbon-water partitioning) is then calculated using the partition coefficients of both species as follows.

$$D_{OC}{}^{PFO(A)} = \frac{1}{1+Ratio} K_{OC}{}^{PFOA} + \frac{Ratio}{1+Ratio} K_{OC}{}^{PFO} \quad \text{(S2)}$$

where $D_{OC}{}^{PFO(A)}$ is the effective K_{OC} considering the relative presence of both forms of the compound and $K_{OC}{}^{PFOA}$ and $K_{OC}{}^{PFO}$ are the K_{OC}s of the neutral and anionic form respectively. The effective K_{AW} of PFO(A) was calculated using only the K_{AW} of the neutral form (PFOA) since the K_{AW} of PFO was assigned a negligible value:

$$D_{AW}{}^{PFO(A)} = \frac{1}{1+Ratio} K_{AW}{}^{PFOA} \quad \text{(S3)}$$

This expression reflects the influence of the ionized species which acts to increase the affinity of the substance for the water phase. PFO does not directly volatilize to the atmosphere in this model, however neutral molecules which volatilize into the atmosphere and partition to non-gaseous phases (e.g. rain, aerosols) can be deprotonated to yield the anion. So, for example, the concentration of PFO in rain is a function of the concentration of PFOA in the gas phase, the K_{AW} of PFOA (partitioning of PFOA into

rain water) and the ratio of PFO:PFOA (reflecting the equilibrium between ionized and neutral form).

S2. Surface ocean exchange (lateral)

The representation of surface ocean exchange in BETR-Global was updated to incorporate data from global drift buoy arrays now available on a 1 x 1^{o} resolution from NOAA (1), www.aoml.noaa.gov/phod/dac/ drifter_climatology.html. The drift buoys consist of a surface and subsurface float attached to a "holey sock" drogue which is centred at a depth of 15 m. The mean current velocity data recorded by these devices reflects the sum of the Ekman (i.e. wind-driven or ageostrophic component) and underlying geostrophic component of the flow but is only representative of the sampling depth (i.e. 0 – 15 m). However, it is possible to decompose the mean surface current velocities into the Ekman/ageostrophic and geostrophic velocity components, as demonstrated in (1). Since the surface flow (Ekman + geostrophic) and geostrophic flow represent upper and lower boundary conditions (Lumpkin R, pers. commun), it is possible to estimate the near-surface current velocities at a given depth as long as the decay in the Ekman component is accounted for. The NOAA website provides mean current velocities (m s^{-1}) for the north-south and east-west components which are presented as a surface velocities (total, 0 – 15 m) and Ekman-removed velocities. Screened data are available for latitude 60^{o}N to 70^{o}S.

The Ekman layer depth (D_E, in m) was estimated using the following simplified equation:

$$D_E = \frac{7.12}{\sqrt{\sin \vartheta}} U_{10} \qquad \text{(S4)}$$

where ϑ is the absolute value of latitude (for $|\vartheta| > 10^{o}$) and U_{10} is the mean wind speed ($m\ s^{-1}$). Mean wind speed for each BETR-Global region was estimated using data from the NCEP/NCAR reanalysis (www.cdc.noaa.gov/cdc/data.ncep.reanalysis.derived.html) over the period 1948 – 2006. The mixed layer depth (MLD) in the model was set to 100 m for all model regions except regions 1 – 48 and 241 – 288 (MLD = 200 m). For depths 0 – 15 m, the surface current velocities can be used directly while the Ekman-removed current velocities can be used directly for depth D_E – 100 m. To simplify the calculations, the Ekman-component was assumed to decay linearly with depth below 15 m and become negligible at the D_E. From this assumption, the mean current velocity over depth 15 – D_E m is simply the average of the surface current velocity and the Ekman-removed current velocity (see Figure S1). The overall mean current velocity for the entire 100 m is then the depth-weighted average of the three values.

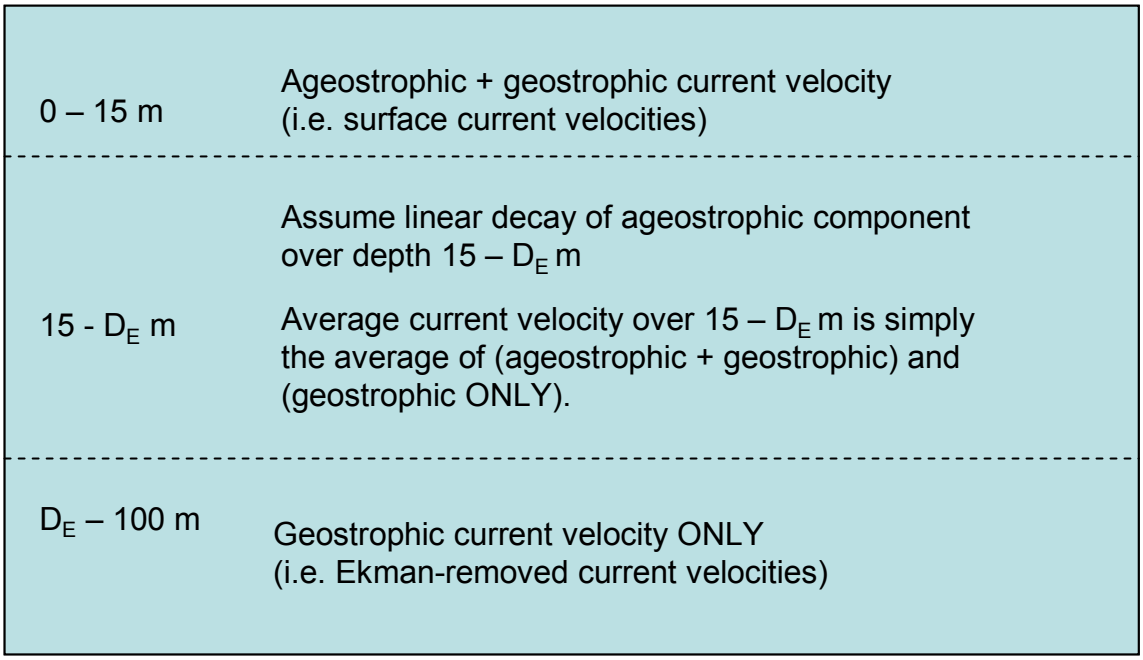

Figure S1. Schematic representation of utilization of mean current velocities taken from the global drift buoy array.

Mean current velocities for latitudes and longitudes representing the borders between regions were extracted from the database. For example, the north/south mean current velocities (m s^{-1}) for region 82/58 (see Figure S2) are represented by the data at 45 ^{o}N between 45 – 30 ^{o}W. The overall mean current velocity for each 1^{o} was then multiplied by the assumed mixed layer depth (m) and the horizontal distance represented by the 1^{o} (m) to arrive at a volumetric flow rate (m^3 s^{-1}). The use of the data in this way results in a representation of time-averaged advective flows. Since the surface ocean compartments were assumed to be well-mixed boxes (over 15 x 15^{o}), the eddy kinetic energy of the ocean was not included as an additional diffusive transport term. The assumption of well-mixed boxes introduces a bias in the sense that emissions entering a given box are instantaneously distributed across the entire geographic region. This assumption results in dilution of the initial source strength and precludes estimation of transport times of a pulse of contaminant. The resulting bias in modeled concentrations in receptor regions (i.e. far-field) is particularly evident for short-term simulations but is reduced substantially as the length of simulation increases (2).

Since drift buoy data were lacking or deemed unreliable, the surface ocean exchange in the Arctic region of the model (regions 1 – 48, see Figure S2) was based on estimates of water inflows/outflows (3, 4), consideration of available Arctic Ocean models (5 – 7), and basic information about the distribution of Pacific and Atlantic-sourced water in this region (8 – 12). Li et al. (5) developed and applied the Arctic Mass Balance Box Model (AMBBM) to model the fate and transport of α-HCH in the Arctic Ocean. AMBBM

divides its 'Arctic Ocean' (defined as waters above 65^{o}N, excluding Baffin Bay, Hudson Bay, the Bering Sea, the Norwegian Sea and the Greenland Sea) into two domains, the North American Arctic Ocean (NAAO) and the Eurasian Arctic Ocean (EAO). The NAAO included waters north of the Bering Strait and 50^{o}W – 180^{o}W whereas the EAO comprised the rest of the surface ocean domain. The NAAO corresponds roughly to BETR-Global regions 1 – 8 and 25 – 32 and is expected to be strongly dominated by waters of Pacific origin over the depth of 0 – 200 m (8, 11). BETR-Global regions 13 – 22, 37 – 46 were assumed to be strongly influenced by waters of Atlantic origin only whereas regions 9 – 12 and 23, 24, 47 and 48 were assumed to be transitional regions (i.e. mixed influence). Flow through the Bering Strait is the most well-known exchange rate and has been estimated in the range of 0.6 – 1 Sv (13). In the BETR-Global model, a value of 0.8 Sv was selected as the default flow from region 49 to region 25. Northward flowing waters from the North Atlantic into the Arctic Ocean are not as well-characterized and estimates vary substantially (e.g. see 3). Atlantic water can enter the Arctic Ocean via the Fram Strait and the Barents Sea (9, 14) and there is some debate over the relative importance of these two routes (7). Using a coupled ice-ocean model of the pan-Arctic region configured at a resolution of 1/12 x 1/12^{o} and 45 depth-levels, Maslowski et al. (7) estimated mean gross flows (1979 – 2001) into the Arctic Ocean of 6.4 Sv through the Fram Strait and 5.9 Sv through the Bear Island Trough into the Barents Sea for the entire depth of the water column. Since BETR-Global explicitly considers only the upper 200 m, the gross northbound flow via the Fram Strait (region 36, 37 to region 12, 13) was assumed to be ~ 4.5 Sv while the gross eastbound flow into the Barents Sea (region 38 eastwards to 39) was assumed to be ~ 3.5 Sv. These volumetric

flows correspond to average current velocities of ~ 0.05 and 0.03 m s^{-1} respectively. The most important gross outflow estimated by Maslowski et al. (7) was ~ 9 Sv via the Fram Strait. This flow was represented in BETR-Global by southward flow across regions 12 and 13 of ~ 7 Sv (upper 200 m only) while the gross flow into the Barents Sea was countered by a reverse flow (region 39 to 38) yielding a net inflow of ~ 2.5 Sv. Due to the spatial resolution of the model, it was problematic to represent ocean circulation within the Arctic Ocean with a great degree of fidelity. Woodgate et al. (15) estimated mean boundary current velocities in the range of 1 – 5 cm s^{-1} in 1995 – 96 in the Eurasian Basin over the depths sampled (1700 m) with mean flow of 2 – 6 cm s^{-1} and episodic currents up to 40 cm s^{-1} measured in the upper water column (at 100 m depth). However, it is difficult to use this information directly. As discussed earlier though, the surface layer of the Arctic Ocean can be crudely represented as two distinct domains, one primarily influenced by Pacific-inflow via the Bering Strait and the other primarily influenced by Atlantic-inflow. Flow between the individual regions can then be estimated as a function of ocean horizontal eddy diffusivity, as was done to derive the surface ocean exchange regime in GloboPOP (16). GloboPOP used the following equation to estimate volumetric exchanges.

$$G_{ij} = \frac{K_X}{L} A_E \qquad \text{(S5)}$$

where G_{ij} is the volumetric flow between region i and j (m^3 s^{-1}), K_X is the horizontal eddy diffusivity (m^2 s^{-1}), L is the path length (m) and A_E is the area of exchange (m^2), which is calculated as a function of mixed layer depth (m) and the length of the surface ocean water interface between the two regions (m). Based on empirical observations, Stewart (17) presented the following equation to estimate K_X.

$$K_X = UL \quad \text{(S6)}$$

where K_X is the horizontal eddy diffusivity ($m^2\ s^{-1}$), U is a constant (0.01±0.005 m s^{-1}) and L is the path length (m). This expression appears to be valid for L ranging from 10 – 1500 km. For BETR-Global, L can be calculated as the square root of the total surface ocean water area (m^2) which varies by latitude and % of the region that is covered by ocean water. However, since L cancels out in Equation S5, U can be viewed as a mass transfer coefficient (L T^{-1}) suggesting an effective water velocity of 0.5 – 1.5 cm s^{-1}. The volumetric flow is then a function of this MTC and the area of exchange. To derive the flow regime for this region of the BETR-Global model, a MTC of 1 cm s^{-1} was initially assumed for exchange between regions in all directions. Flow between regions representing the boundary of the NAAO and EAO (e.g. region 22, 23) were reduced (U ~ 0.1 cm s^{-1}). In this way, contaminants are distributed through the NAAO and EAO without becoming well-mixed over the time period of the simulation. Where data were available, flows through certain regions (e.g. ~ 2 Sv through the Canadian Archipelago, Prinsenberg, S.J. (18); Davis Strait, ~ 2 ± 1.0 Sv northward, 4.6 ± 1.1 Sv southward, Cuny et al., (19)) were represented as well as possible.

S3. Deep water formation

Deep water formation was represented by including the estimated sinking fluxes provided by Lohmann et al. (20). The data from Lohmann et al. was also compared to information provided in Kahana et al. (21). The regions considered by Lohmann et al. (20) to have relevant deep water formation were the Norwegian Sea (68°N – 80°N, 0 – 25°E, 10 Sv, where 1 Sv = 10^6 m^3 s^{-1}), the Labrador Sea (50°N – 60°N, 60°W – 40°W, 5 Sv), the

Weddell Sea (60°S – 85°S, 70°W – 20°W, 11 Sv) and the Ross Sea (60°S – 80°S, 170°E – 155°W, 10 Sv). The total sinking fluxes were apportioned to the corresponding BETR-Global regions (see Figure S2). For all other BETR-Global regions, the default surface – deep water exchange mass transfer coefficients (m h^{-1}) from GloboPOP (16) for the appropriate latitudinal band were used. These MTCs are multiplied by the surface area of the ocean compartment (m^2) to arrive at a volumetric exchange rate. Based on these assumptions, the mixing time of the deep ocean (estimated from total ocean surface area and assumed average deep ocean depth of 3600 m) due to surface-deep water exchange was ~ 650 years, in agreement with published estimates (500 – 1500 years, see Johanneson & Burdige (22))

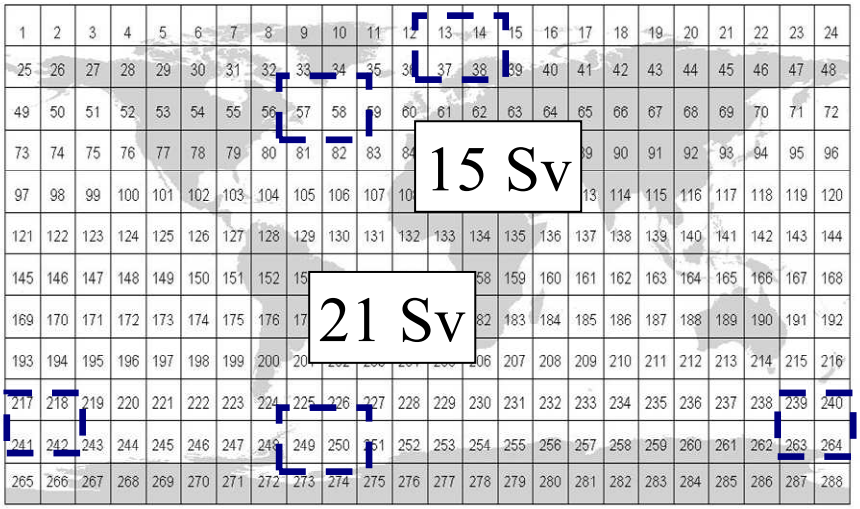

Figure S2. Regions with enhanced surface-deep water exchange as suggested by Lohmann et al (20).

Once all horizontal and vertical flows were estimated, it was important to ensure that a water mass balance was established (i.e. water flow in = water flow out). The median ratio of water in:water out based on the drift buoy data for the model domain was 0.95

(IQR = 0.75 – 1.21). To obtain a complete mass balance, the iterative algorithm proposed by Woodfine et al. (23) was adapted for use with the BETR-Global flow matrices. In this procedure, the proportion of flow in each direction is calculated using the input flow regime. These proportions are held constant and then total volume fluxes across the entire flow matrix are adjusted to arrive at a complete water mass balance. The average adjustment factor for the Arctic Ocean regions was 1.4 while the overall average adjustment factor for the entire flow regime was 1.5. While in some cases the flows may have increased/decreased more substantially, the general features of the flow regime are maintained and the more serious error related to water mass imbalances is eliminated.

S4. Preliminary Model Simulations

Since it was unclear whether the simplified exchange regime adequately captured the desired features, in particular the domains of Atlantic and Pacific-influence, the model was evaluated in two ways. First, the long-term fate and transport of iodine-129 (I-129) into the Arctic Oceans from sources in the North Sea was used to test the reasonableness of the surface ocean exchange parameterization. Alfimov et al. (6) modeled the fate and transport of I-129 into the Arctic Ocean over the period 1950 – 2010 using a modified version of the ANWAP RAIG model (13). I-129 is emitted from two nuclear reprocessing facilities at Sellafield, UK and La Hague, France. Since these locations were outside the model domain, Alfimov et al. (6) generated an emission function for the Norwegian Sea which accounts for the time delay for transport from source to this region. This emission function was used as the source term for the BETR-Global simulations and was directed into region 37 (see Figure S2). Modeled concentrations in the Arctic

regions of the model were compared to observations (24, 25) in different locations of the Arctic (e.g. Western Arctic Basins, Eastern Arctic Basins, Barents Sea) from 1993 and 2001 (see Figure S3).

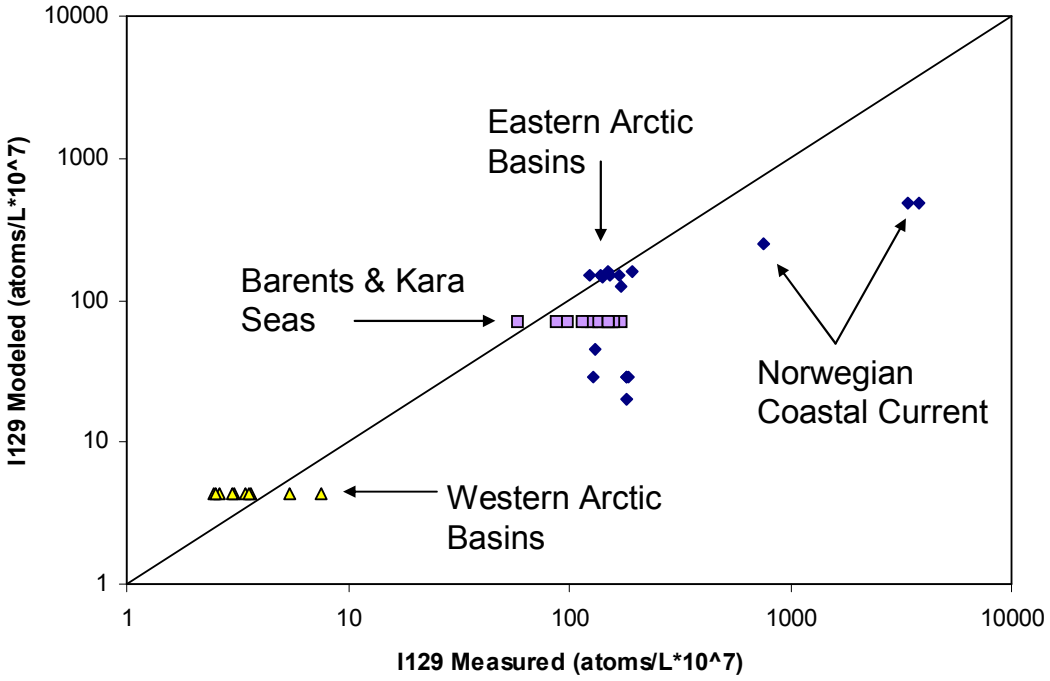

Figure S3. Modeled (BETR-Global) versus observed concentrations of I-129 in 1993 (Western Arctic Basins, Barents & Kara Seas) and 2001 (Norwegian Coastal Current, Eastern Arctic Basins)

Transport of Atlantic-sourced I-129 to Western Arctic Basin surface water (0 – 200 m) is known to be limited (14, 24). This feature of Arctic Ocean circulation appears to be well-represented by the BETR-Global model. There is also good agreement overall between modeled and observed concentrations in the Barents Sea and Eastern Arctic Basins. Concentrations in the Norwegian Coastal Current are under-predicted but this result is not surprising since all ocean regions are assumed to be well-mixed (hence diluting the emissions which might otherwise be largely entrained in a smaller volume of water).

Another series of model simulations were conducted using the single-species version of BETR-Global and the physical-chemical properties of the anion only. Here, emissions from each major source region (Europe/Russia, North America, Asia; see section S5) were simulated separately. These simulations allow the contribution of each source region to the total modeled concentration in every region to be assessed. For the Arctic region of the model (regions 1 – 48), these simulations give an indication of the extent to which emissions from North America and Europe contaminate the various regions of the Arctic Ocean. Simulations were conducted from 1950 – 2010 and model results for 2005 are presented in Figure S4.

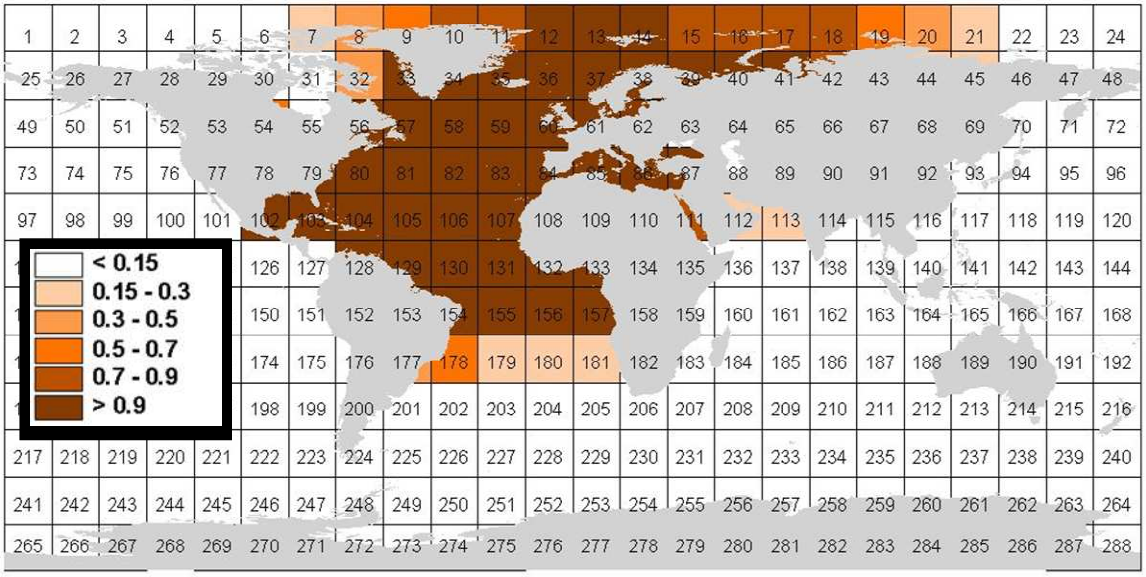

Figure S4. Contribution (%) to total modeled concentrations in the surface ocean compartment from North American + Europe emissions. The contribution from Asian sources is equal to [1 – (the displayed values)].

As shown in Figure S4, emissions from North American and Europe/Russia are largely confined to what would be considered the Eastern Arctic Ocean (EAO) in AMBBM developed by Li et al. (5). Overall, these model simulations confirm that the desired

features of ocean circulation within the Arctic Ocean are broadly represented, given the coarse resolution of the model.

S5. Supporting Information for Emission Estimates

Global Distribution of Emissions. Will et al. (26) compiled information on the type of fluoropolymer produced, production process and estimated production capacity for more than 30 manufacturing facilities. Each site was assigned to the appropriate model region based on the longitude and latitude of the facility. Fluoropolymer (FP) production facilities using APFO are located in the United States (regions 78 – 80; see Figure S2), Europe (regions 60 – 62, 85), Russia (region 64) and Asia (regions 92 – 94, 114 – 116). The total production capacity of facilities (26) in each model region was used as the primary basis to apportion the total estimated historic emissions of APFO emitted as a result of FP manufacturing. This simplifying assumption means that emissions per unit FP produced are identical across all sites. In Prevedouros et al (27), APFO production (and hence emissions from direct sources) was estimated for four periods (1951 – 1964, 1965 – 1979, 1980 – 1994, 1995 – 2002). Since the majority of FP plants have not been operational since 1951, emissions assigned to each region were adjusted accordingly. However, complete historical emission estimates are currently available for only one FP production site in the United States (28). To address this data gap, information on temporal trends (1970s – present) in overall FP production in the United States and Europe compiled by Will et al. (26) was considered. Other sources included patent submissions (see (27)), voluntary disclosures to regulatory agencies by manufacturers (29 – 31) and company websites detailing corporate history.

With respect to the direct manufacture of APFO, the ECF process was estimated to account for 80 – 90% of the historical production with the largest manufacturing sites in the United States and Belgium (27). Significant ECF production capacity was developed in Italy and to a lesser extent, Japan. Beginning in 1975, additional production capacity based on direct oxidation of perfluorooctyl iodide (27) came online at one site in Germany and at least one site in Japan. Note that this production process, estimated to account for the remaining 10 – 20% of historical production, yields exclusively linear isomers. While there is some information on emissions from the facilities in the United States (30), no information about other locations was found in the public domain. Based on available information and expert opinion, all emissions from 1951 – 1964 were assumed to occur in the United States (region 78). From 1965 – 1974, 75% of emissions occurred in the United States (regions 78, 79) and 25% in Europe (regions 61, 85). After 1975, approximately 50% of total historic emissions were assigned to locations in the United States (regions 78, 79), 40% to locations in Europe (regions 61, 85) and 10% to locations in Japan (region 94).

The resulting temporal trends in emissions of APFO and the associated emission of PFO(A) from the two main direct sources in North America, Europe/Russia and East Asia are below (Figure S5a-c). Note that emissions in Europe/Russia were assumed to begin in 1965 while emissions in North America and Asia were assumed to begin in 1951.

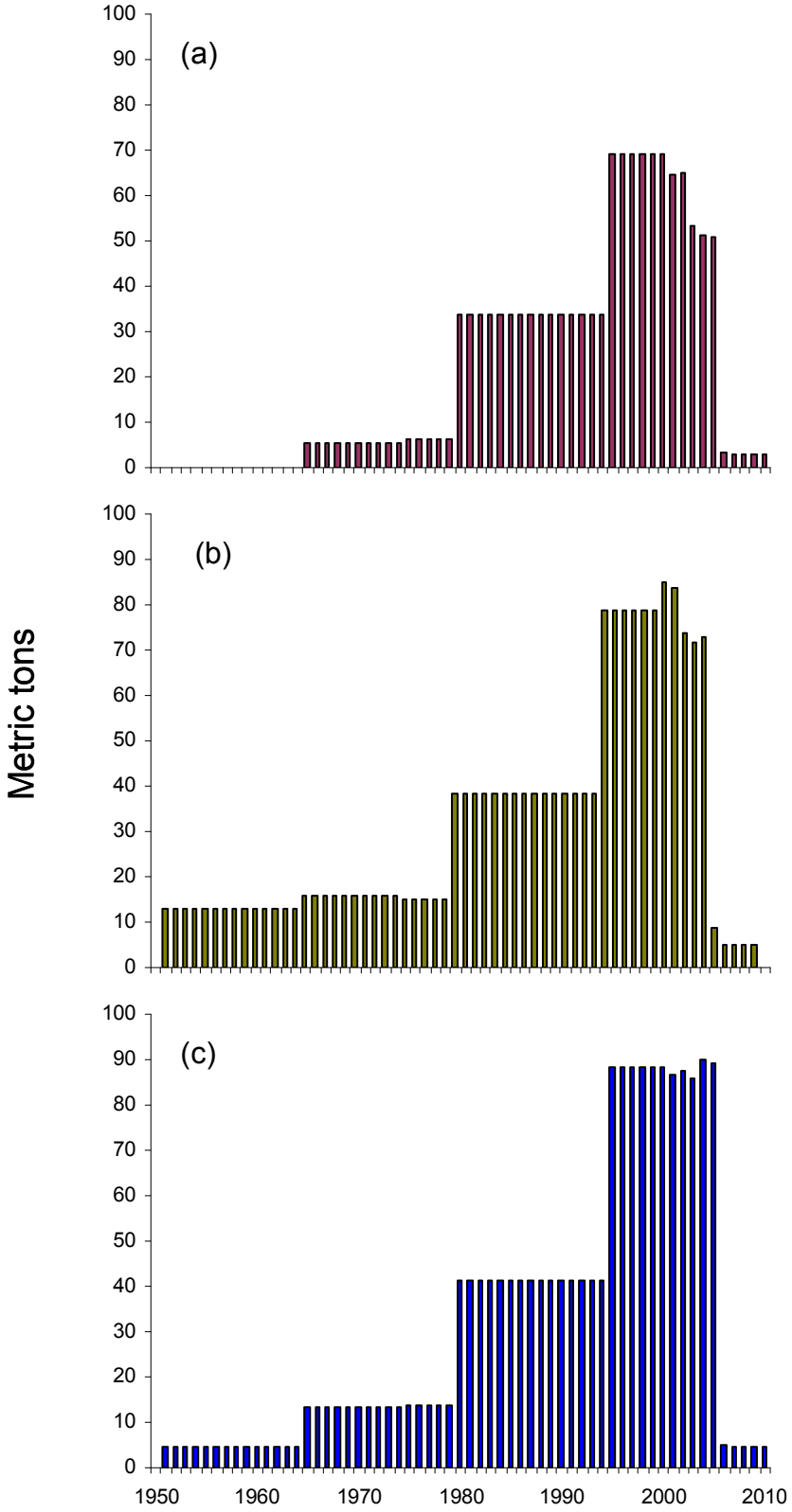

Figure S5. Emission estimates of APFO (metric tons) from 1950 – 2010 for (a) Europe/Russia, (b) North America and (c) Asia.

Comparision between source inventories and production data

Will et al. (26) reported estimates of historic production of PTFE and other FPs manufactured using APFO (e.g. FEP, PFA) in the United States over the period 1970 – 2004. In Prevedouros et al. (27), 60% of the APFO used in FP manufacturing was assumed to be released to the environment and total APFO production estimates were used as the basis for estimating total emissions. Since the amount of APFO required per unit production FP is not likely to be constant over time (due to production efficiency improvements, improved APFO recovery/recycling), a direct relationships between FP production and APFO emissions cannot be expected. However, it is still useful to compare the relative FP production to the relative APFO emissions used in the current simulations. This comparison is shown in Figure S6.

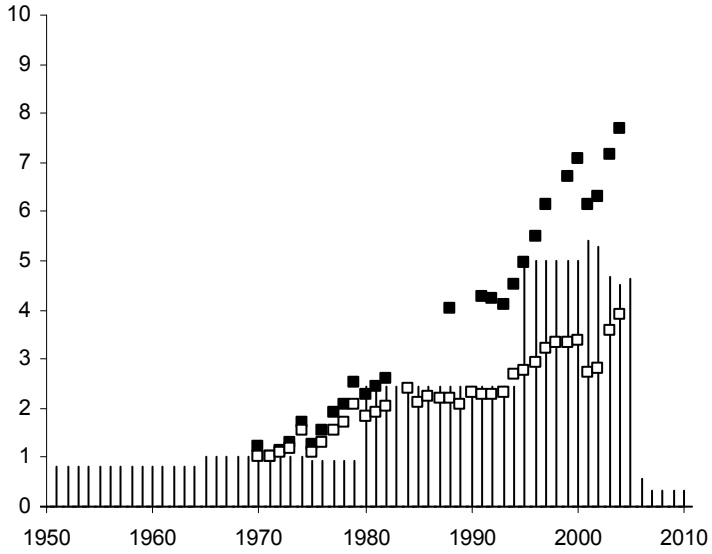

Figure S6. PTFE (open squares) and total FP production (closed squares) in the United States relative to 1970 over the period 1970 – 2004 in comparison to APFO emission estimates from FP production (bars) in the United States relative to 1970.

As shown in Figure S6, PTFE production increased approximately 4-fold over the period 1970 – 2004 while total FP production increased approximately 8-fold. In comparison, APFO emissions from FP production increased by a factor of 5 over the same period illustrating the reasonable overlap between estimated FP production and APFO emissions related to FP manufacturing activity over the same time period.

More detailed information on historic emissions from a single FP manufacturing facility in the United States (DuPont Washington Works) was reported by Paustenbach et al. (28). The amount of APFO used by the plant was based on accounting records while releases were based on information from APFO mass balances for the production lines as contained in internal DuPont documents (which are not available to the general public however). The DuPont Washington Works FP facility is located in BETR-Global region 79 and is the only FP facility assigned to that region. Therefore, it is possible to make a direct comparison between emission estimates reported in Paustenbach et al. (28) and the emission estimates derived from Prevedouros et al. (27), as shown in Figure S7.

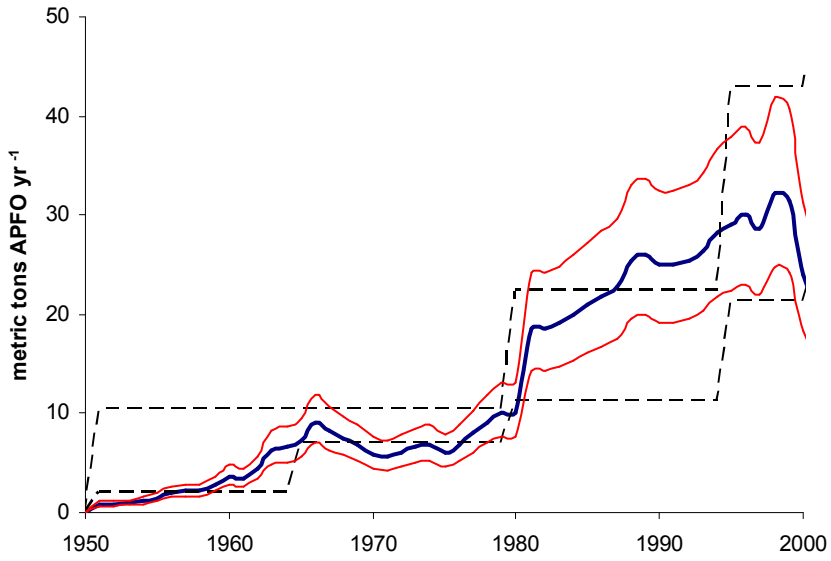

Figure S7. Estimated emissions of APFO (1950 – 2000, in metric tons yr^{-1}) taken from Paustenbach et al. (29) (blue line) ± 30% estimated uncertainty (red lines) versus minimum and maximum emission estimates (dotted lines) derived from Prevedouros et al. (28) for BETR-Global region 79, FP production

The total estimated releases under the minimum and maximum scenario from 1950 – 2000 are ~ 440 and 900 metric tons respectively whereas the total estimated emissions based on Paustenbach et al. (28) are ~ 660 metric tons (505 – 855). While the maximum emission scenario substantially overestimates the reported emissions from 1950 – 1965, reported emissions from 1985 – 1995 appear to be underestimated by up to 50%. However, considering the uncertainties inherent to all emission inventory estimations, the overall agreement between the two emission functions is acceptable.

S6. Summary tables and additional figures of model outputs

Summary tables and additional figures characterizing various atmospheric model outputs are presented in the following section.

Table S1 – Modeled gross deposition fluxes (ng m^{-2}) in the year 2005 for regions representing North America, below 60 ^{o}N, assuming $pK_a = 0$ (see Figure S2). Note that modeled values were similar for the period 2000 – 2005 and that the gross deposition flux in source regions (78 – 80) assuming No E to Air were not calculated using model output, since they are assumed to be equivalent to yearly emissions to air.

	With Emissions to Air					No Emissions to Air				
BETR	< 1%	25%	50%	75%	> 99%	< 1%	25%	50%	75%	> 99%
52	57	54	51	49	81	*neg.*	*neg.*	*neg.*	*neg.*	*neg.*
53	49	46	44	42	51	*neg.*	*neg.*	*neg.*	*neg.*	*neg.*
54	41	40	38	37	52	*neg.*	*neg.*	*neg.*	*neg.*	*neg.*
55	117	114	111	109	121	*neg.*	*neg.*	*neg.*	*neg.*	*neg.*
56	71	69	66	64	86	*neg.*	*neg.*	*neg.*	*neg.*	*neg.*
57	77	73	69	66	83	*neg.*	*neg.*	*neg.*	*neg.*	*neg.*
76	57	55	52	50	65	*neg.*	*neg.*	*neg.*	*neg.*	*neg.*
77	24	24	24	25	38	*neg.*	*neg.*	*neg.*	*neg.*	*neg.*
78*	99	107	114	120	142					
79*	962	1005	1046	1084	1140			NOT CALCULATED		
80*	665	655	647	639	531					
101	18	18	18	18	29	*neg.*	*neg.*	*neg.*	*neg.*	*neg.*
102	13	14	14	15	22	*neg.*	*neg.*	*neg.*	*neg.*	*neg.*
103	55	54	52	50	61	*neg.*	*neg.*	*neg.*	*neg.*	*neg.*
127	22	21	20	18	25	*neg.*	*neg.*	*neg.*	*neg.*	*neg.*
AVERAGE	155	157	158	159	168			NOT CALCULATED		
***Source**	575	589	602	614	605					
Non-Source	50	49	47	45	59	*neg.*	*neg.*	*neg.*	*neg.*	*neg.*

Table S2 – Modeled gross deposition fluxes (ng m^{-2}) in the year 2005 for regions representing North America, below 60 ^{o}N, assuming $pK_a = 1.5$ (see Figure S2). Note that modeled values were similar for the period 2000 – 2005 and that the gross deposition flux in source regions (78 – 80) assuming No E to Air were not calculated using model output, since they are assumed to be equivalent to yearly emissions to air.

	With Emissions to Air					No Emissions to Air				
BETR	< 1%	25%	50%	75%	> 99%	< 1%	25%	50%	75%	> 99%
52	72	71	69	69	87	2	2	2	2	2
53	62	61	60	59	53	2	2	2	2	1
54	51	51	51	51	55	1	1	1	1	1
55	133	131	129	127	123	5	5	5	5	5
56	87	86	83	80	93	3	3	3	3	3
57	94	90	88	87	86	3	3	3	3	3
76	72	71	70	70	66	2	2	2	2	2
77	30	31	32	34	40	1	1	1	1	1
78*	107	117	126	134	150					
79*	1000	1047	1092	1133	1182			NOT CALCULATED		
80*	614	591	569	548	540					
101	23	23	24	24	31	1	1	1	1	1
102	16	17	19	20	25	1	1	1	1	1
103	64	62	60	59	65	2	2	2	2	2
127	27	26	24	23	27	1	1	1	1	1
AVERAGE	163	165	166	168	175			NOT CALCULATED		
***Source**	574	585	596	605	624					
Non-Source	61	60	59	59	63	2	2	2	2	2

Table S3 – Modeled gross deposition fluxes (ng m^{-2}) in the year 2005 for regions representing North America, below 60 ^{o}N, assuming $pK_a = 3.5$ (see Figure S2). Note that modeled values were similar for the period 2000 – 2005 and that the gross deposition flux in source regions (78 – 80) assuming No E to Air were not calculated using model output, since they are assumed to be equivalent to yearly emissions to air.

	With Emissions to Air					No Emissions to Air				
BETR	< 1%	25%	50%	75%	> 99%	< 1%	25%	50%	75%	> 99%
52	514	363	281	230	195	253	197	160	134	116
53	224	187	162	144	130	108	98	88	80	73
54	253	201	173	154	141	123	107	96	88	82
55	482	426	399	381	372	283	282	279	274	273
56	221	289	285	268	252	123	177	182	175	167
57	488	351	280	235	205	263	210	175	151	134
76	318	219	175	149	130	156	119	100	87	78
77	118	108	100	93	88	57	57	55	53	51
78*	145	300	384	416	438					
79*	814	1882	2643	3215	3530		NOT CALCULATED			
80*	672	989	1132	1202	1262					
101	158	104	82	70	62	73	53	44	39	36
102	185	130	116	113	114	108	91	90	92	97
103	188	218	202	186	165	106	139	137	131	119
127	262	142	95	72	58	125	75	53	42	35
AVERAGE	336	394	434	462	476		NOT CALCULATED			
***Source**	544	1057	1386	1611	1744					
Non-Source	284	228	196	175	159	148	134	122	112	105

Table S4 – Modeled concentrations in source regions in the lower atmosphere (pg m^{-3}), precipitation levels (ng L^{-1}) and gross deposition flux to the Arctic region (kg yr^{-1}) for 2005, assuming $pK_a = 0$. Note that modeled values were similar for the period 2000 – 2005. Modeled air concentrations in source regions (78 – 80) assuming No E to Air reflect the extent of volatilization from terrestrial surfaces. Precipitation levels under this mode of entry assumption were not calculated (NC) using model output.

		Lower Atmosphere (pg m^{-3})		Precipitation (ng L^{-1})		Gross Deposition Flux to Arctic (kg yr^{-1})		
	BETR	E direct to air	No E to air	E direct to air	No E to air	BETR	E direct to air	No E to air
< 1%	78 - 80	1.2 - 6.5	≤ 0.01	0.05 - 0.5	NC	1 - 24	244	0.2
	60 - 62	0.7 - 3.6	≤ 0.01	0.25 - 1.6		1 - 48	1542	1.4
	92 - 94	1.0 - 4.2	≤ 0.01	0.25 - 1.3				
25%	78 - 80	1.1 - 6.3	≤ 0.01	0.05 - 0.5	NC	1 - 24	239	0.2
	60 - 62	0.7 - 3.6	≤ 0.01	0.24 - 1.5		1 - 48	1479	1.3
	92 - 94	1.0 - 4.1	≤ 0.01	0.24 - 1.3				
50%	78 - 80	1.1 - 6.1	≤ 0.01	0.04 - 0.4	NC	1 - 24	234	0.2
	60 - 62	0.7 - 3.5	≤ 0.01	0.23 - 1.5		1 - 48	1419	1.3
	92 - 94	0.9 - 4.0	≤ 0.01	0.23 - 1.2				
75%	78 - 80	1.0 - 5.8	≤ 0.01	0.04 - 0.4	NC	1 - 24	229	0.2
	60 - 62	0.6 - 3.4	≤ 0.01	0.23 - 1.4		1 - 48	1367	1.3
	92 - 94	0.9 - 3.9	≤ 0.01	0.22 - 1.2				
> 99%	78 - 80	1.1 - 5.8	≤ 0.01	0.04 - 0.4	NC	1 - 24	354	0.3
	60 - 62	1.0 - 4.7	≤ 0.01	0.16 - 0.7		1 - 48	1852	1.6
	92 - 94	1.4 - 5.4	≤ 0.01	0.22 - 0.9				

Table S5 – Modeled concentrations in source regions in the lower atmosphere (pg m^{-3}), precipitation levels (ng L^{-1}) and gross deposition flux to the Arctic region (kg yr^{-1}) for 2005, assuming $pK_a = 1.5$. Note that modeled values were similar for the period 2000 – 2005. Modeled air concentrations in source regions (78 – 80) assuming No E to Air reflect the extent of volatilization from terrestrial surfaces. Precipitation levels under this mode of entry assumption were not calculated (NC) using model output.

		Lower Atmosphere (pg m^{-3})		Precipitation (ng L^{-1})		Gross Deposition Flux to Arctic (kg yr^{-1})		
	BETR	E direct to air	No E to air	E direct to air	No E to air	BETR	E direct to air	No E to air
< 1%	78 - 80	1.3 - 6.8	< 0.5	0.06 - 0.4		1 - 24	307	7
	60 - 62	0.9 - 4.8	< 0.5	0.22 - 1.1	NC	1 - 48	1954	54
	92 - 94	1.5 - 4.9	< 0.5	0.35 - 1.2				
25%	78 - 80	1.2 - 6.6	< 0.5	0.05 - 0.4		1 - 24	310	7
	60 - 62	1.0 - 4.8	< 0.5	0.20 - 1.0	NC	1 - 48	1923	54
	92 - 94	1.5 - 5.0	< 0.5	0.32 - 1.1				
50%	78 - 80	1.2 - 6.3	< 0.5	0.05 - 0.4		1 - 24	312	7
	60 - 62	1.0 - 4.8	< 0.5	0.18 - 0.9	NC	1 - 48	1900	53
	92 - 94	1.5 - 5.2	< 0.5	0.28 - 1.0				
75%	78 - 80	1.1 - 6.1	< 0.5	0.05 - 0.4		1 - 24	317	7
	60 - 62	1.0 - 4.8	< 0.5	0.17 - 0.8	NC	1 - 48	1869	52
	92 - 94	1.5 - 5.3	< 0.5	0.25 - 0.9				
> 99%	78 - 80	1.1 - 6.0	< 0.5	0.05 - 0.4		1 - 24	378	8
	60 - 62	1.1 - 4.9	< 0.5	0.16 - 0.7	NC	1 - 48	1948	51
	92 - 94	1.5 - 5.5	< 0.5	0.22 - 0.8				

Table S6 – Modeled concentrations in source regions in the lower atmosphere (pg m^{-3}), precipitation levels (ng L^{-1}) and gross deposition flux to the Arctic region (kg yr^{-1}) for 2005, assuming $pK_a = 3.5$. Note that modeled values were similar for the period 2000 – 2005. Modeled air concentrations in source regions (78 – 80) assuming No E to Air reflect the extent of volatilization from terrestrial surfaces. Precipitation levels under this mode of entry assumption were not calculated (NC) using model output.

		Lower Atmosphere (pg m^{-3})		Precipitation (ng L^{-1})		Gross Deposition Flux to Arctic (kg yr^{-1})		
	BETR	E direct to air	No E to air	E direct to air	No E to air	BETR	E direct to air	No E to air
< 1%	78 - 80	9 - 32	6 - 26	0.02 - 0.08		1 - 24	2526	1184
	60 - 62	8 - 24	4 - 17	0.02 - 0.06	NC	1 - 48	10109	5016
	92 - 94	9 - 19	6 - 10	0.03 - 0.05				
25%	78 - 80	5 - 26	4 - 22	0.21 - 1.0		1 - 24	1543	799
	60 - 62	4 - 18	2 - 13	0.15 - 0.7	NC	1 - 48	7406	4111
	92 - 94	6 - 13	4 - 7	0.22 - 0.5				
50%	78 - 80	4 - 22	3 - 18	0.21 - 1.4		1 - 24	1153	631
	60 - 62	3 - 15	2 - 11	0.20 - 1.1	NC	1 - 48	6094	3584
	92 - 94	5 - 10	3 - 6	0.34 - 0.8				
75%	78 - 80	4 - 19	3 - 16	0.17 - 1.2		1 - 24	938	531
	60 - 62	2 - 13	1 - 10	0.23 - 1.5	NC	1 - 48	5266	3205
	92 - 94	4 - 9	3 - 5	0.42 - 1.0				
> 99%	78 - 80	3 - 18	2 - 15	0.16 - 1.1		1 - 24	801	465
	60 - 62	2 - 12	1 - 9	0.25 - 1.8	NC	1 - 48	4691	2921
	92 - 94	3 - 7	2 - 4	0.48 - 1.1				

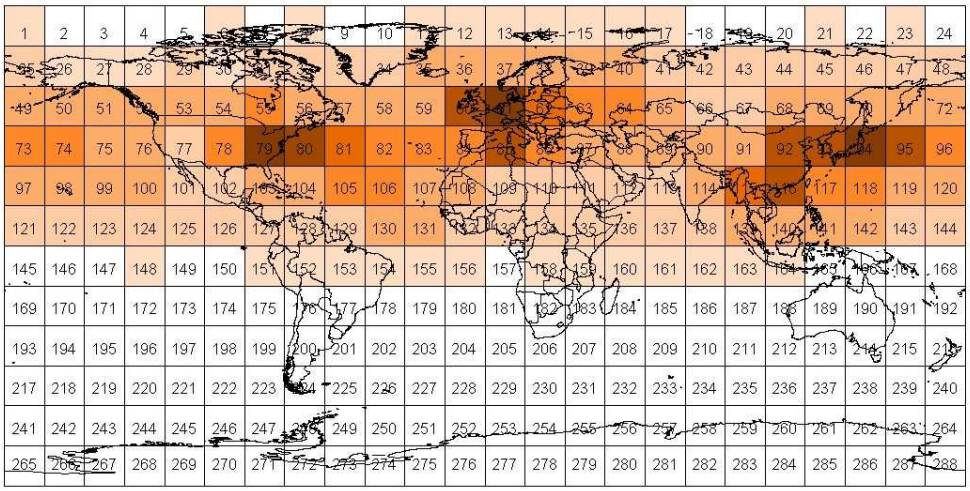

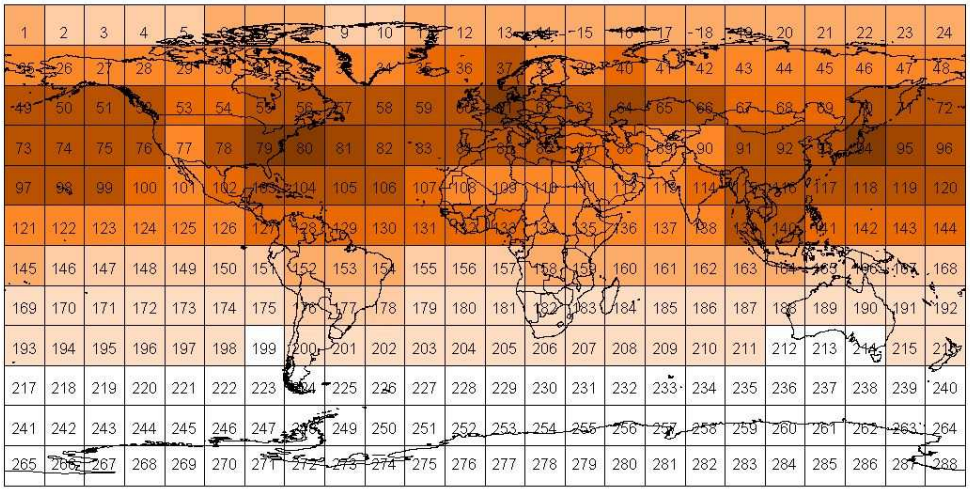

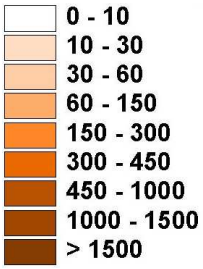

Figure S8. Gross deposition flux (kg yr^{-1}, see legend) in 2005 assuming emissions to air, ϕ = 25% and pK_a = 0 (top map) and pK_a = 3.5 (bottom map).

S7. Marine aerosol flux of PFO(A)

There has been some speculation in the literature as to importance of marine aerosols for the transport of PFCAs (27, 32). Marine aerosols are produced in the world's oceans and contribute significantly to the global aerosol load. Most of the focus of research on marine aerosols has been on sea salt aerosols, which are the most abundant natural atmospheric aerosol in terms of mass. Sea salt aerosols are generated from bubbles bursting at the sea surface producing "film" droplets (0.5 – 5 μm) and "jet" droplets (3 – 50 μm) or when high winds tear larger "spume" droplets (>20 μm) off the wave crests (33). Research has recently shown that that submicron marine aerosols (<1 μm) can also make an important contribution to the total marine aerosol flux (34). The chemical composition of the aerosol has been shown to change with aerosol size with a clear transition from saline for the larger particles to almost entirely organic particles for the smaller fractions of marine aerosols (35). An important parameter that will determine the long range potential of the marine aerosols is the atmospheric residence time. For large particles (1.0 – 10 μm) the residence time is of the order of hours to a few days and is essentially determined by sedimentation and dry deposition (33). These large particles are saline in nature and will have only short range atmospheric transport potential, nicely illustrated in the work of Benassai et al. (36), who demonstrated that sea salt aerosol depositional fluxes decreased inland by two orders of magnitude in the first 200 km distance from the sea. The smaller more organic-rich particles (0.05 – 1.0 μm; the so-called accumulation mode) have a residence time of many days, mostly determined by removal through wet deposition (33) and will have considerable long range atmospheric transport potential. Spatially resolved global production fluxes (mg m^{-2} d^{-1}) of marine

aerosols have been estimated for total marine aerosols of differing size fractions (0.03 – 25 μm) (37) and also for accumulation mode marine aerosols only (0.1 – 0.5 μm) (34). Estimated global sea salt aerosol production fluxes were on average 24 mg m^{-2} d^{-1} and peaked at a value of 420 mg m^{-2} d^{-1} (37). Estimated global accumulation mode sea-spray aerosol production fluxes were much lower and peaked at 6.0 mg m^{-2} d^{-1} (34).

Here we attempt to estimate the amount of PFO(A) that could be associated with these aerosol production fluxes. To calculate the concentration of PFO(A) on marine aerosol particles it is necessary to multiply PFO(A) concentrations in surface ocean water with an enrichment factor (EF) (35), as it has been long understood that certain organic materials are enriched at the air water interface (38). Enrichment factors for PFO(A) in the surface microlayer of coastal waters were reported to range from 1.2 – 1.8 (39) while McMurdo et al. (32) reported an EF of 55.7 for PFO(A) in seawater measured in the laboratory. Another study reported an EF of 3 for PFO(A) in foam generated in a laboratory (40). The gross flux of PFO(A) ($F_{PFO(A)}$) on marine aerosols (kg m^{-2} $year^{-1}$) ejected from the ocean surface can be calculated using equation S7.

$$F_{PFO(A)} = [PFO(A)](EF)(F_{\phi})(3.65x10^{-19}) \quad \text{(S7)}$$

where [PFO(A)] is the ocean water concentration of PFO(A) (pg L^{-1}), EF is the enrichment factor for PFO(A) in the surface microlayer/marine aerosols, $F_{Ø}$ is the marine aerosol production flux (mg m^{-2} d^{-1}) and the factor 3.65 x 10^{-19} is to convert $F_{PFO(A)}$ into the correct units. We assume that the marine aerosol has the same density as the seawater. This flux can be used to estimate mass flows of PFO(A) from the ocean to the atmosphere by multiplying by the surface area of the ocean being considered. Studies

over the period 2002 – 2005 measuring the concentrations of PFO(A) in surface seawater (cited in the main article) report seawater concentrations from <20 (in remote ocean regions) to 1060 pg L^{-1} (in a polluted coastal region offshore Japan). We estimate a PFO(A) flux from ocean to atmosphere for the Northern Hemisphere (NH) using the average value for $F_{Ø}$ of 24 mg m^{-2} d^{-1} (which includes both coarse and accumulation mode aerosols), an EF of 55.7, the NH observed open ocean water concentration range (<20 – 439 pg L^{-1}) and NH ocean surface area (1.53 x 10^{14} m^2). This calculation results in a gross mass flow of <1.5 to 33 kg $year^{-1}$ PFO(A) for the entire hemisphere. Assuming the average EF reported in (39) of 1.4, the estimated mass flow is reduced to <0.04 – 0.84 kg $year^{-1}$. The potential for this PFO(A) to undergo long range transport depends on the fate of the marine aerosols themselves and the fate of the PFO(A) associated with the marine aerosols. For example, McMurdo et al. (32) concluded that a significant fraction of PFO(A) associated with aerosols will be released into the gas phase. However, even if we assume that 100% of the PFO(A) associated with newly ejected marine aerosols is released into the gas phase, the mass of PFO(A) is insignificant compared to estimated global stack emissions in 2005 (20 – 45 metric tons). In terms of LRT to the Arctic, our estimated total PFO(A) mass flux from marine aerosol generation is also lower than modeled gross deposition fluxes related to transport and degradation of FTOHs (113 – 226 kg yr^{-1} (41); 50 – 500 kg yr-1 (42) in 2005) and measurements (114 – 587 kg in 2005 (43)). In conclusion, we find that long-range transport of PFO(A) associated with marine aerosol generation is not likely to be an important transport process. However, we encourage others to challenge and refine these calculations using more sophisticated approaches.

Literature Cited

1. Lumpkin, R.; Garraffo, Z. Evaluating the decomposition of tropical Atlantic drifter observations. *J. Atmos. Oceanic Techn. I* **2005**, 22, 1403 – 1415.
2. Iosjpe, M.; Brown, J.; Strand, P. Modified approach to modeling radiological consequences from releases into the marine environment. *J. Environ. Radioact.* **2002**, 60, 91 – 103.
3. Vowinckel, E.; Orvig, S. Water balance and heat flow of the Arctic Ocean. *Arctic* **1962**, 15, 205 – 223.
4. Ingvaldsen, R.; Loeng, H.; Asplin, L. Variability in the Atlantic inflow to the Barents Sea based on a one-year time series from moored current meters. *Cont. Shelf Res.* **2002**, 22, 505 – 519.
5. Li, Y.F.; Macdonald, R.W.; Ma, J.M.; Hung, H.; Venkatesh, S. Historical α-HCH budget in the Arctic Ocean: the Arctic Mass Balance Box Model (AMBBM). *Sci. Tot. Environ.* **2004**, 324, 115 – 139.
6. Alfimov, V.; Possnert, G.; Aldahan, A. Anthropogenic iodine-129 in the Arctic Ocean and Nordic Seas: Numerical modeling and prognoses. Mar. Pollut. Bull. **2006**, 52, 380 – 385.
7. Maslowski, W.; Marble, D.; Walczowski, W.; Schaeur, U.; Clement, J.L.; Stemtner, A.J. On climatological mass, heat, and salt transports through the Barents Sea and Fram Strait from a pan-Arctic coupled ice-ocean model simulation. *J. Geophys. Res.* **2004**, 109, C03032.

8. Jones, E.P.; Anderson, L.G.; Swift, J.H. Distribution of Atlantic and Pacific waters in the upper Arctic Ocean: Implications for circulation. *Geophys. Res. Lett.* **1998**, 25, 765 – 768.
9. Jones, E.P. Circulation in the Arctic Ocean. *Polar Res.* **2001**, 20, 139 – 146.
10. Jones, E.P.; Swift, J.H.; Anderson, L.G.; Lipizier, M.; Civitarese, G.; Falkner, K.K.; Kattner, G.; McLaughlin, F. Tracing Pacific water in the North Atlantic Ocean. *J. Geophys. Res.* **2003**, C4, 3116.
11. Rudels, B.; Anderson, L.G.; Jones, E.P. Formation and evolution of the surface mixed layer and halocline of the Arctic Ocean. *J. Geophys. Res.* **1996**, 101, C4, 8807 – 8821.
12. Rudels, B.; Jones, E.P.; Schauer, U.; Eriksson, P. Atlantic sources of the Arctic Ocean surface and halocline waters. *Polar Res.* **2004**, 23, 181 – 208.
13. Arctic Nuclear Waste Assessment Program (ANWAP). Radionuclides in the Arctic Seas from the Former Soviet Union: Potential health and ecological risks. Layton, D.; Edson, R.; Varela, M.; Napier, B (Eds), Tech. Rep. By ANWAP, Office of Naval Research (ONR), 1997.
14. Carmack, E.C.; Aagaard, K.; Swift, J.H.; Macdonald, R.W.; McLaughlin, F.A.; Jones, E.P.; Perkin, R.G.; Smith, J.N.; Ellis, K.M.; Killius, L.R. Changes in temperature and tracer distributions within the Arctic Ocean: results from the 1994 Arctic Ocean section. *Deep-Sea Res. II* **1997**, 44, 1487 – 1502.
15. Woodgate, R.A.; Aagaard, K.; Muench, R.D.; Gunn, J.; Björk, G.; Rudels, B.; Roach, A.T.; Schauer, U. The Arctic Ocean boundary current along the Eurasian slope and

adjacent Lomonosov Ridge: Water mass properties, transports and transformations from moored instruments. *Deep-Sea Res. I* **2001**, 48, 1757 – 1792.

16. Wania, F.; Mackay, D. Global chemical fate of alpha-hexachlorocyclohexane. 2. Use of a global distribution model for mass balancing, source apportionment, and trend prediction. *Environ. Toxicol. Chem*. **1999**, 18, 1400-1407.
17. Stewart, R.H. Introduction to Physical Oceanography. Department of Oceanography, Texas A & M University, **2005**. Available online at http://oceanworld.tamu.edu/ resources/ocng_textbook/contents.html
18. Prinsenberg, S.J. Volume, heat and freshwater fluxes through the Canadian Arctic Archipelago: Present understanding and future research plans. Bedford Institute of Oceanograpy, Nova Scotia, Canada, **1998**. Available at http://www.mar.dfo-mpo.gc.ca/science/ocean/seaice/Publications/prins12.pdf
19. Cuny, J.; Rhines, P.B.; Kwok, R. David Strait volume, freshwater and heat fluxes. *Deep Sea Res I* **2005,** 52, 519 – 542.
20. Lohmann, R.; Jurado, E.; Pilson, M.E.Q.; Dachs, J. Oceanic deep water formation as a sink of persistent organic pollutants. *Geophys. Res. Lett.* **2006**, 33, L12607.
21. Kahana, R.; Bigg, G.R.; Wadley, M.R. Global ocean circulation modes derived from a multiple box model. *J. Phys. Oceanog*. **2004**, 34, 1811 – 1823.
22. Johannesson, K.H.; Burdige, D.J. Balancing the global oceanic neodymium budget: Evaluating the role of groundwater. *Earth Planet. Sci. Lett.* **2007**, 253, 129 – 142.

23. Woodfine, D.G.; MacLeod, M.; Mackay, D.; Brimacombe, J.R. Development of continental scale multimedia contaminant fate models: Integrating GIS. *Environ. Sci. Pollut. Res.* **2001**, 8, 164 – 172.

24. Smith, J.N.; Ellis, K.M.; Kilius, L.R. ^{129}I and ^{137}Cs tracer measurements in the Arctic Ocean. *Deep-Sea Res. I* **1998**, 45, 959 – 984.

25. Alfimov, V.; Aldahan, A.; Possnert, G.; Winsor, P. Anthropogenic iodine-129 in seawater along a transect from the Norwegian coastal current to the North Pole. Mar. Pollut. Bull. **2004**, 49, 1097 – 1104.

26. Will, R.; Kälin, T.; Kishi, A. Fluoropolymers. In CEH Marketing Research Report October 2005; SRI International: Menlo Park, CA, 2005.

27. Prevedouros, K.; Cousins, I. T.; Buck, R. C.; Korzeniowski, S. H. Sources, fate and transport of perfluorocarboxylates. *Environ. Sci. Technol*. **2006**, 40 (1), 32-44.

28. Paustenbach, D.J.; Panko, J.M.; Scott, P.K.; Unice, K.M. A methodology for estimating human exposure to perfluorooctanoic acid (PFOA): A retrospective exposure assessment of a community (1951 – 2003). *J. Toxicol. Environ. Health, Part A* **2007**, 70, 28 – 57.

29. E. I. du Pont de Nemours and Company. Voluntary use and exposure information profile: Ammonium perfluorooctanoate (APFO). AR 226-0599, US EPA HQ-OPPT-2002-0051.

30. 3M Company. Voluntary Use and Exposure Information Profile: Perfluorooctanoic Acid and Salts. AR 226-0595, US EPA HQ-OPPT-2002-0051.

31. Fluoropolymers Manufacturing Group (FMG). FMG Presentation to EPA, April 26, 2002, Sanitized Copy. AR 226-1094, US EPA HQ-OPPT-2002-0051.

32. McMurdo, C.J.; Ellis, D.A.; Webster, E.; Butler, J.; Christensen, R.D.; Reid, L.K. Aerosol enrichment of the surfactant PFO and mediation of the water - air transport of gaseous PFOA. *Environ. Sci. Technol*., **2008**, 42, 3969-3974.

33. Zakey, A.S.; Giorgi, F.; Bi, X. Modeling of sea salt in a regional climate model: fluxes and radiative forcing. *J. Geophys. Res*. **2008**, 113, D14221.

34. Scannell, C.; O'Dowd, C.D. **2007.** A global emission inventory of submicron sea-spray aerosols. In Nucleation Atmospheric Aerosols. C.D. O'Dowd and P.E. Wagner (Eds), Springer, pp. 1079-1082.

35. Oppo, C..; Bellandi, S.; Degli Innocenti, N.; Stortini, A.M.; Loglio, G.; Schiavuta, E.; Cini, R. Surfactant components of marine organic matter as agents for biogeochemical fractionation and pollutant transport via marine aerosols. *Mar. Chem*. **1999**, 63, 235-253.

36. Benassai, S.; Becagli, S.; Gragnani, R.; Magand, O.; Proposito, M.; Fattori, I.; Traversi, R.; Udisti, R. Sea-spray deposition in Antarctic coastal and plateau areas from ITASE traverses. *Ann. Glaciol*., **2005**, 41, 32-40.

37. Grini, A.; Myhre, G.; Sundet, J.K.; Isaksen, I.S.A. Modeling the annual cycle of sea salt in the global 3D model Oslo CTM2: Concentrations, fluxes and radiative impact. *J. Clim*., **2002**, 15, 1717-1730.

38. Blanchard, D.C.; Syzdek, L.D. Bubble tube - apparatus for determining rate of collection of bacteria by an air bubble rising in water. *Limnol. Ocean*. **1974**, 19, 133-138.

39. Ju, X.; Jin, Y.; Sasaki, K.; Saito, N. Perfluorinated substances in surface, subsurface water and microlayer from Dalian coastal waters in China. *Environ. Sci. Technol*. **2008**, 42, 3538 – 3542.

40. Kaiser, M. A.; Barton, C. A.; Botelho, M.; Buck, R. C.; Buxton, L.W.; Gannon, J.; Kao, C.-P. C.; Larsen, B. S.; Russell, M. H.; Wang,N.; Waterland, R. L. Understanding the transport of anthropogenic fluorinated compounds in the environment. *Organohalogen Compd*. **2006**, 68, 675-678.

41. Schenker, U.; Scheringer, M.; MacLeod, M.; Martin, J.W.; Cousins, I.T.; Hungerbühler, K. Contribution of volatile precursor substances to the flux of perfluorooctanoate to the Arctic. *Environ. Sci. Technol* **2008***, 42*, 3710 – 3716.

42. Yarwood, G.; Kemball-Cook, S.; Keinath, M.; Waterland, R.L.; Korzeniowski, S.H.; Buck, R.C.; Russell, M.H.; Washburn, S.T. High-resolution atmospheric modeling of fluorotelomer alcohols and perfluorocarboxylic acids in the North American troposphere. *Environ. Sci. Technol.* **2007**, 41, 5756 – 5762.

43. Young, C.J.; Furdui, V.I.; Franklin, J.; Koerner, R.M.; Muir, D.C.G.; Mabury, S.A. Perfluorinated acids in Arctic snow: New evidence for atmospheric formation. *Environ. Sci. Technol.* **2007**, 41, 3455 – 3461.